research paper

Whole-nanoparticle atomistic modeling of the schwertmannite structure from total scattering data

M. Sestu,[a] G. Navarra,[a] S. Carrero,[b,c] S. M. Valvidares,[d] G. Aquilanti,[e] R. Pérez-Lopez[b] and A. Fernandez-Martinez[c]

[a]Dipartimento di Scienze Chimiche e Geologiche, Università degli Studi di Cagliari, SS 554 bivio per Sestu, Monserrato, Cagliari 09042, Italy, [b]Department of Geology, University of Huelva, Campus 'El Carmen', Huelva 21071, Spain, [c]ISTerre, Univ., Grenoble-Alpes, CNRS, Grenoble F-38000, France, [d]ALBA Synchrotron Light Source, Cerdanyola del Vallés, Barcelona E-08290, Spain, and [e]Sincrotrone Trieste, ELETTRA, Basovizza (TS), 34012, Italy

Schwertmannite is a poorly crystalline nanometric iron sulfate oxyhydroxide. This mineral shows a structural variability under different environments. Because of that, the determination of its structure and, consequently, of its physical–chemical properties is quite challenging. This article presents a detailed structural investigation of the structure of schwertmannite conducted under different approaches: X-ray absorption spectroscopy, Rietveld refinement, and a combined reverse Monte Carlo and Debye function analysis of the whole nanoparticle structure. The schwertmannite model presented here is, to the auhors' knowledge, the most complete model so far reported.

1. Introduction

Schwertmannite is a poorly crystalline iron sulfate oxy-hydroxide occurring in ochreous precipitates from acid-sulfate-rich water (Bigham *et al.*, 1990). Schwertmannite precipitates as the result of natural or anthropogenic neutra-lization of acid and rock mine drainage. Schwertmannite was first recognized as a mineral in the 1990s (Bigham *et al.*, 1994). Its formation is usually associated with the presence of the iron minerals goethite (α-FeOOH) and jarosite [$KFe_3(SO_4)_2(OH)_6$] (Burton *et al.*, 2008; Regensburg *et al.*, 2004; Wang *et al.*, 2006). Its texture consists of small aggregates with 'hedgehog' morphology, including large amounts of amor-phous content and characterized by needles with a coherent structural domain of 30–40 Å (French *et al.*, 2012). The stoi-chiometry depends on the sulfur content: the formula is $Fe_8O_8(OH)_{8-2x}(SO_4)_x$ with x ranging from 1 to 1.75 (Bigham *et al.*, 1996).

Owing to the poorly crystalline nature and the nanometric size of this mineral, the determination of its atomic structure appears quite challenging. The first structural model was proposed by Bigham *et al.* (1994). On the basis of the simila-rities between their X-ray diffraction (XRD) patterns, infrared absorption data and Mossbauer spectroscopy data, the authors suggested that schwertmannite is isostructural with akaganeite (Deore *et al.*, 2005), with sulfate groups replacing chloride anions. This model was supported by a pair distri-bution function (PDF) study of synchrotron powder diffrac-tion data and by density functional theory analyses (Fernandez-Martinez *et al.*, 2010). These authors addressed the description of the structure by hypothesizing two possible arrangements for the sulfate group, one in which it shares two O atoms with the Fe–O network (forming a complex with an
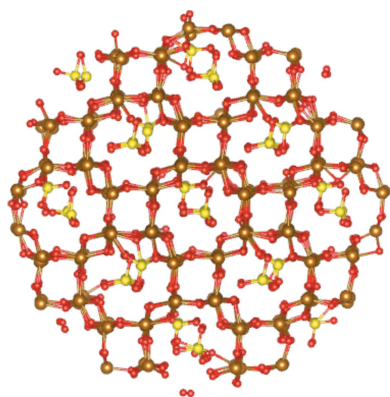
inner-sphere sulfate ligand, 'IS sulfate'), and another where it is connected to the octahedra *via* a hydrogen bond (forming an electrostatically bound complex with an outer-sphere sulfate ligand, 'OS sulfate'). Two different structural models were proposed for the iron octahedral framework, which, as the authors suggested, may be merely two solutions that fit the PDF data, but not the only possible solutions. This result is in agreement with the study of French *et al.* (2012), who suggested that the nanocrystalline structure of schwertmannite cannot be described by a single unit cell. In contrast to these previous studies, an electron nanodiffraction study on synthetic schwertmannite did not show evidence for an akaganeite-like structure, whereas similarities were found with two-line ferrihydrite (Loan *et al.*, 2004). This relationship was supported by results obtained by Hockridge *et al.* (2009) using high-resolution transmission electron microscopy (HRTEM) analysis. The authors proposed that schwertmannite has a ferrihydrite-like core with needles of goethite nucleating from the core. More recently, French *et al.* (2012) reported HRTEM analyses that contrast with those of Hockridge and co-workers, using a different synthetic approach and demonstrating the elusive nature of this iron oxyhydroxide.

As a further example supporting the ambiguous identity of this mineral, a wide range of values for the solubility product K_{sp} covering several orders of magnitude have been reported (Bigham *et al.*, 1996; Yu *et al.*, 1999; Kawano & Tomita, 2001; Sánchez-España *et al.*, 2011). This fact has been recently highlighted by Caraballo *et al.* (2013) in an exhaustive study on the solubility product for 30 natural samples, where a range of $\log K_{sp}$ values from 5.8 to 39.5 is reported. Depending on the chemical environment, in terms of pH and pe, different statistical predictive equations were adopted to calculate the best $\log K_{sp}$.

The structural study of natural nanoparticles poses various problems that are related to their inherent small sizes, their disordered structure and the structural variability that they present under different environments (Caraballo *et al.*, 2015). While for crystalline materials the coherent scattering included in the diffraction peaks contains enough information to solve the structure, the use of so-called total scattering techniques is necessary to study materials with diffraction patterns containing a large amount of diffuse scattering (Egami & Billinge, 2003; Billinge & Kanatzidis, 2004). Techniques based on the use of the Debye equation for reciprocal space analyses, or the PDF for analyses in real space, or combinations of the two, are used in these cases. The study of the structure of schwertmannite by Fernandez-Martinez *et al.* (2010) is a good and pertinent example of how analyses in real and reciprocal space give complementary information; while the PDF is useful to refine the local order of the iron octahedral framework, the analysis of the low-Q peaks in the XRD pattern allowed the authors to refine the positions of sulfate in the structure. However, and in spite of the recent advances in the field of PDF software and modeling, the structural study of defective nanoparticles remains a difficult task because of the lack of specific modeling approaches. While reverse Monte Carlo (RMC) approaches are systematically used now to analyze scattering data from amorphous materials and liquids (McGreevy & Pusztai, 1988) and Rietveld analysis is performed to study coherently scattered radiation from crystals, there is a lack of methods available for the study of solids whose diffraction patterns consist of broad Bragg peaks and a non-negligible fraction of diffuse scattering. The case of schwertmannite is paradigmatic: while the only structure proposed is based on a unit-cell model, some authors have proposed from TEM observations that schwertmannite is a polyphasic material, with a high degree of heterogeneity (French *et al.*, 2012). This also means that proposing a single structural model based on a unit cell is not meaningful for these natural nanoparticles (Gilbert *et al.*, 2013). New analysis methods are thus required, which combine the use of statistical methods of analysis such as RMC to explore the configurational space in detail, with the use of constraints to prevent non-physical solutions.

In the present work a detailed structural investigation of the structure of schwertmannite is conducted by using an RMC model of a whole nanoparticle structure. This approach allows us to introduce a higher degree of disorder and to account for a variety of plausible structural motifs in a single model. This method is combined with X-ray absorption spectroscopy (XAS), Rietveld refinement (Rietveld, 1969) and Debye equation analyses (Debye, 1915). Sulfur K-edge XAS was used to ascertain the local environment of the sulfate in our natural and synthetic schwertmannite samples, complementing previous work by Wang *et al.* (2015). The validity of the model proposed by Bigham *et al.* (1994) and refined by Fernandez-Martinez *et al.* (2010) was verified by Rietveld and RMC analysis.

Although the Debye scattering equation (DSE) was introduced in 1915 (Debye, 1915), its use has been limited because of the high computational effort needed to model nanometre-sized particles explicitly. The development of more performant CPUs has only recently allowed a wider application of this formula for the calculation of the diffraction patterns of finite-sized particles (Hall, 2000; Cervellino *et al.*, 2003, 2006). Further improvements in terms of computing time saving have been achieved by some authors (Gelisio *et al.*, 2010; Antonov *et al.*, 2012) by running the calculation of the DSE on graphics processing units (GPUs).

In our work a refined model was obtained by randomly moving the atoms from their starting position, *i.e.* a whole atomistic version of the Fernandez-Martinez *et al.* (2010) akaganeite-like model. According to the RMC method the moves were accepted or not on the basis of the agreement between calculated and experimental data (McGreevy *et al.*, 1988). In particular, diffraction scattering data both in the real and in the reciprocal space were compared: DSE running on GPUs is used to calculate the structure factor $S(Q)$ and the PDF is calculated by applying the Fourier transform (FT) to $S(Q)$. The same approach was recently used in the study of the debated structure of ferrihydrite (Gilbert *et al.*, 2013), although the calculation of the DSE was classically performed on a CPU.

Complementary results were obtained using both Rietveld and RMC/DSE refinements: Rietveld refinement returns a refined unit cell in a periodic crystal lattice; RMC/DSE refinement returns a disordered particle model in which atomic displacements were applied without any symmetry restraint. This ambivalent point of view gives a deeper comprehension of the structure of nanosized and poorly crystalline materials, such as schwertmannite, which are neither proper crystals nor amorphous phases, and whose structure elucidation remains challenging (Caraballo *et al.*, 2015).

Altogether, the three techniques permitted a global study of the structure of schwertmannite: the position of the sulfate group within the channels of the akaganeite-like structure was examined and the possibility of the presence of other FeOOH phases, which can affect the experimental data, was also explored. The presence of goethite was considered in response to previous work (French *et al.*, 2014). An intimate structural relationship between the structures of goethite and schwertmannite has been already described by Fernandez-Martinez *et al.* (2010). The conversion of schwertmannite into goethite would be achievable by a simple topotactic transformation involving the relocation of iron octahedra from the structure of schwertmannite (Fernandez-Martinez *et al.*, 2010). We anticipate that, as a result of our structural investigation, a small amount of goethite will be found in the diffuse scattering even if it is not recognizable in the X-ray powder diffraction (XRPD) pattern. The presence of other phases is crucial for the determination of physical–chemical parameters such as the solubility product, which, if not appropriately taken into account, could lead to misinterpretation of experimental data.

2. Materials and methods

2.1. Samples and high-energy X-ray scattering data collection for Rietveld and RMC/DSE analysis

The schwertmannite reciprocal- and real-space X-ray diffraction data were the same as used for the Fernandez-Martinez *et al.* (2010) study. Both natural and synthetic samples were used. In brief, natural samples were taken as fresh precipitates from the acid drainage in the Monte Romero mine (Huelva, Spain). Sample Nat-Air was air-dried, while sample Nat-Freeze was freeze-dried. Sample SynHT was synthesized by dissolving $Fe_2(SO_4)_3$ in deionized water at 358 K for 1 h using the procedure described by Loan *et al.* (2004). The precipitate was vacuum filtered and freeze-dried to complete dryness using a VirTis Benchtop freeze-dryer (Hucoa-Erlöss). Sample Syn was synthesized at 333 K from ferric chloride and sodium sulfate solutions following the methods reported by Schwertmann & Cornell (1991).

High-energy X-ray diffraction measurements were carried out at beamline ID15B at the European Synchrotron Radiation Facility using monochromatic X-rays with an energy of ~87 keV (0.1419 Å) in Debye–Scherrer geometry. Samples were loaded into 0.8 mm-diameter polyimide capillaries that were sealed with wax. The beamline was calibrated using a CeO$_2$ standard (NIST 679b) for the data collection of the sample SynHT and using an Ni standard for the data collection of samples Syn, Nat-Air and Nat-Freeze. An LaB$_6$ standard was also measured to determine instrumental resolution effects. The diffraction patterns were collected using a MARCCD165 two-dimensional (sample SynHT) and a Pixium 4700 (samples Syn, Nat-Air and Nat-Freeze) detector. Measurements of the samples, the empty capillary and the background were performed at ambient temperature in a Q range of 1–25 Å^{-1}. Corrections for sample–detector distance, tilt angle of the detector with respect to the direction of the incident radiation and polarization were performed using the software *Fit2D* (Hammersley *et al.*, 1996; Hammersley, 2016). Total scattering structure factors and PDFs were obtained using the software *PDFGetX2* (Qiu *et al.*, 2004).

2.2. Mineral synthesis for XAS experiments

Synthetic schwertmannite was obtained using the procedure described by Loan *et al.* (2004). Briefly, 2.506 g of $Fe_2(SO_4)_3$, previously dehydrated, was mixed with 1 l of Milli-Q water, preheated at 358 K, and stirred for 1 h. The precipitate was collected by vacuum filtration through a 0.45 μm nylon membrane filter and washed several times with pure water.

The jarosite standard was synthesized by mixing 180 ml of 5 M KOH and 100 ml of 1 M Fe(NO$_3$)$_2$ (Schwertmann & Cornell, 1991). The suspension was diluted to 2 l with Milli-Q ultrapure water and aged at 343 K for 60 h. The resulting suspension was washed several times with Milli-Q ultrapure water.

Copiapite, $Fe_5(SO_4)_6(OH)_2 \cdot 20(H_2O)$, and halotrichite, $FeAl_2(SO_4)_4 \cdot 22H_2O$, were obtained from Excalibur Minerals (Charlottesville, VA, USA), and their structures were checked by X-ray diffraction (see supporting information).

Both natural and synthetic minerals were lyophilized to complete dryness using a VirTis Benchtop freeze-dryer (Hucoa-Erlöss, Spain). Mineralogical characterization was performed with XRPD using a Bruker D8 Advance diffractometer with $K\alpha$ radiation. The sample was scanned from 2 to 70° in 2θ with 0.02° steps and a counting time of 5 s per step. Moreover, the precipitates were chemically analyzed after acid digestion with HNO$_3$ for determination of major and trace elements by inductively coupled plasma–atomic emission spectroscopy (Jobin Yvon Ultimate 2) at the University of Huelva.

2.3. XAS experiments

X-ray absorption near-edge structure (XANES) experiments were performed at the BOREAS (BL29) beamline of the ALBA synchrotron light source (Barla *et al.*, 2016). X-ray photon-energy scans from 2450 to 2510 eV were taken across the sulfur K-edge region at an energy resolution estimated at 0.15 eV (1200 lines per mm grating, 30 μm vertical gap monochromator slits) and with X-ray polarization adjusted to be linear in the horizontal plane. Spectra were acquired in 'on-the-fly' grating rotation mode, taken at intervals of about 2 min with an approximate 0.1 eV step size and 0.1 s counting

time. Data were collected at room temperature in total electron yield mode by measuring the sample drain currents with a Keithley K428 current amplifier, for which powders of the samples were fixed on conductive graphite tape and mounted in an ultra-high-vacuum chamber.

Extended X-ray absorption fine structure (EXAFS) data were collected at the XAFS (11.1) beamline of the Elettra synchrotron light source (Cicco *et al.*, 2009). Powder samples were suspended in a cyclohexane solution, filtered off with 0.1 μm cellulose membrane filters, dried at room temperature and deposited on cellulose membranes. Room-temperature sulfur *K*-edge (2485 eV) EXAFS spectra were collected in fluorescence mode using a silicon drift detector (KETEK GmbH AXAS-M with an area of 80 mm^2). An Si(111) double-crystal monochromator was used with about 0.3 eV resolution at 2.5 keV. Higher-order harmonics were effectively eliminated by using a double-flat silica mirror placed at a grazing angle of 8 mrad. The intensity of the monochromatic X-ray beam before the sample was measured by a 30 cm-long ionization chamber detector, filled with a mixture of 30 mbar of N_2 and 1970 mbar of He (1 bar = 10^5 Pa). EXAFS data were scanned in an energy range from 2300 to 3220 eV. In the XANES region, equidistant energy steps of 0.2 eV were used, whereas for the EXAFS region, equidistant *k* steps of 0.03 Å^{-1} eV were adopted with an integration time of 10 s per point.

3. Data treatment and modeling

3.1. XAS data analysis

Energy calibration, background fitting and normalization of EXAFS and XANES spectra were performed with *Athena* (Newville, 2001; Ravel & Newville, 2005). *Artemis* (Newville, 2001; Ravel & Newville, 2005) was used to perform fits to the EXAFS data from schwertmannite models constructed from the Fernandez-Martinez *et al.* (2010) proposed structure. The statistical F-test (Joyner *et al.*, 1987; Michalowicz *et al.*, 1999) was used to determine the statistical significance of each of the hypotheses made, which consisted of different numbers of shells of backscattering atoms around the photoabsorber, and therefore of different numbers of fitting parameters. Only those models which improved the fit between theoretical and experimental EXAFS spectra at the 90% level of confidence were considered.

3.2. Rietveld refinement

Rietveld fitting was performed using the program *Maud* (Ferrari & Lutterotti, 1994). The schwertmannite unit cell proposed by Fernandez-Martinez *et al.* (2010) was chosen as starting model. The cell exhibits a triclinic structure with akaganeite-like channels hosting the sulfate groups. Sulfate groups occupy four different positions in the Fernandez-Martinez *et al.* (2010) model, with two sulfates forming outer-sphere complexes and the other two in inner-sphere complexes. Here, a unit cell with eight sites for sulfates has been considered in order to allow the possibility that the

sulfate groups can be distributed in a way different from that described by Fernandez-Martinez *et al.* (2010). Four of them share two oxygen atoms with the iron atoms, forming the channels (IS sulfates); the remaining four are placed in the center of the channel and are bonded with the FeOOH network *via* hydrogen bonds (OS sulfates). In this model the resulting stoichiometry is $Fe_8O_8(OH)_6(SO_4)_2$, since each sulfate site has an occupancy equal to 0.5.

The presence of goethite is hypothesized on the basis of literature data and of the identification of a peak at Q = 1.5 Å^{-1} in the experimental XRPD pattern, characteristic of α-FeOOH (Burton *et al.*, 2008). Both the schwertmannite and goethite models were included in the refinement procedure. The starting models for goethite and schwertmannite are the structures reported, respectively, by Gualtieri & Venturelli (1999) and Fernandez-Martinez *et al.* (2010). Two fits were performed on each sample, the first considering only the presence of schwertmannite, the second allowing also the presence of goethite. The following refinement strategy was applied:

(1) The starting diffraction pattern was calculated considering a spherically shaped schwertmannite domain with a diameter of 40 Å and applying a scale factor in such a way that the intensity of the calculated pattern is roughly comparable to that of the experimental data.

(2) A first refinement step was performed with the scale factor, the background (estimated with a fourth-degree polynomial) and the 2θ offset as fitting parameters. In the case where the presence of goethite was considered, the concentration of the two phases was also refined.

(3) A second step was performed including the domain size and the cell parameters. Finally, the sulfate occupancies were optimized. Some constraints are imposed: the occupancy of the oxygen atom in a sulfate group is equal to the occupancy of the bonded sulfur; the sum of the sulfur occupancies must be equal to 4; the occupancy of the inner sulfate is equal to 1 minus the occupancy of the outer sulfate. In this way, only four degrees of freedom are added to the system. In the refinement of the goethite cell parameters the ratio *c/a* was also constrained as constant, in order to avoid uncontrolled structure deformation.

No further parameters were involved in the refinement in order to avoid a large number of degrees of freedom.

3.3. RMC/DSE refinement

A code for RMC/DSE refinements was specifically written in order to model a three-dimensional finite-sized particle. The positions of the atoms in the particle were iteratively modified depending on the agreement of the calculated $S(Q)$ and PDF with the corresponding experimental data. During an RMC cycle an atom is randomly chosen and randomly moved from its position within a maximum displacement. A constraint on the minimum distance between two atoms is imposed in order to avoid physical inconsistency of the models. After each move $S(Q)$ is calculated using the DSE on an Nvidia Ge-Force GTX 690 GPU. The PDF is calculated by applying the FT to the
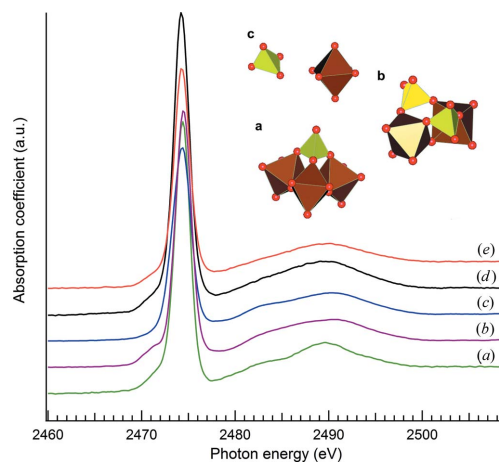
Figure 1
K-edge S XANES spectra of (*a*) jarosite, (*b*) copiapite, (*c*) halotrichite, and (*d*) synthetic and (*e*) natural schwertmannite. The atomistic models show the bonding environment of sulfate (yellow tetrahedra) in the three reference minerals. Red spheres are O atoms; brown polyhedra are FeO_6 octahedra.

$S(Q)$. The two calculated functions are compared with the corresponding experimental data through an agreement parameter and each move is accepted depending on the improvement of the agreement parameter. The RMC/DSE refinement continues until convergence.

In the cases considering the presence of goethite, the positions of the atoms of both schwertmannite and goethite models were refined. The partial contribution of schwertmannite and goethite to the global $S(Q)$ and, then, to the PDF was estimated before the RMC/DSE iteration procedure started by linear fitting (GSL libraries were used; Galassi *et al.*, 2009). Schwertmannite and goethite particles were generated by cutting a 30 Å sphere from supercells of the two structures and terminating all the surface atoms with oxygen. Further details on the code are reported in the supporting information.

4. Results and discussion

4.1. XAS

4.1.1. Schwertmannite S XANES.
S K-edge XANES spectra for both natural and synthetic schwertmannite, as well as for the reference compounds, are shown in Fig. 1. The observed

energy shift confirms that the oxidation state in all phases studied was S^{VI}, sulfate (SO_4^{2-}), with a tetrahedral coordination. Previous studies have shown that sulfur K-edge XANES spectra can be used as a fingerprinting method to determine the coordination environment of this element in Fe-bearing mineral structures (Myneni, 2000). In particular, the presence of a pre-edge peak (pre-peak) is indicative of covalent bonding between the sulfate group and the octahedral iron framework. The spectra for halotrichite, a structure in which the sulfate group does not share any O atoms with the iron octahedra, shows no appreciable pre-peak. In contrast, this pre-peak is present in the jarosite (three O atoms shared between the sulfate and iron octahedra) and copiapite (two shared O atoms) spectra. The XANES spectra for the natural and synthetic schwertmannite are identical and also show the presence of this pre-peak, suggesting a similar S coordination environment to jarosite or copiapite, *i.e.* covalent binding to the iron structure. The post-edge region of the XANES spectrum shows slightly different features. Attempts to perform linear combination fitting of the schwertmannite spectra using the references were not conclusive, mostly because of the strong similarity between the post-edge features of the different minerals. The results from these XANES analyses confirm that at least some of the sulfate in the schwertmannite structure is IS sulfate.

4.1.2. Schwertmannite S EXAFS.
Sulfur K-edge EXAFS spectra of synthetic and natural schwertmannite are shown in Fig. 2. The Fourier-transformed EXAFS spectra showed only one significant peak, corresponding to the S—O interatomic distance (1.48 Å) with a coordination number close to the theoretical value of 4, which was fixed to 3.8 in some of the fits (see Table 1). Attempts were made to include a second shell of Fe atoms, in accordance with the information obtained from XANES spectra that indicates the formation of IS complexes. A binuclear bidentate complex was built from the defective structure of schwertmannite, following Fernandez-Martinez *et al.* (2010), with a sulfate group bonded in contact with a vacant Fe site. These attempts needed the inclusion of a single scattering S—O_O path between the photoabsorber and an oxygen atom from the Fe—O octahedron, and a single scattering from the Fe atom. The results are given in Table 1 (where subscript O denotes octahedral and T tetrahedral). The distances are compatible with the model. Only the coordination number of the S—O_O path is higher than the theoretical one. The reason
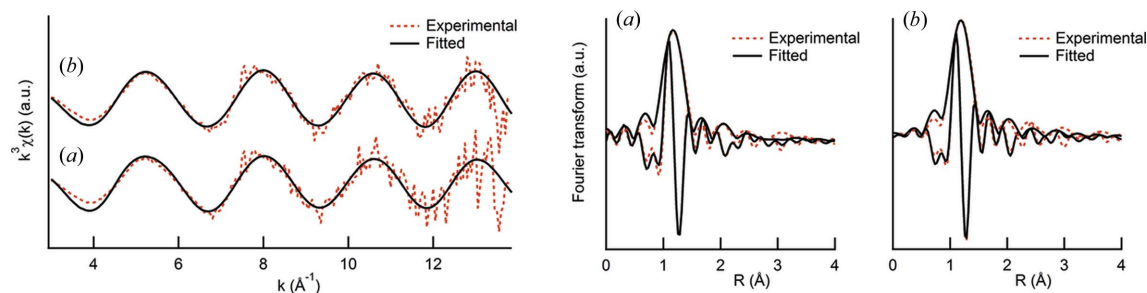

Figure 2
S K-edge EXAFS spectra (left) and real and imaginary parts of their Fourier transform (right) in (*a*) natural and (*b*) synthetic schwertmannite. Only the fit corresponding to the first shell of oxygen neighbors at 1.48 Å is shown. This corresponds to sulfate in outer-sphere positions.

Table 1
Results of the EXAFS fitting using different structural models, including sulfate in the outer-sphere position (only $S-O_T$ path) and in the inner-sphere position (with $S-Fe$ and $S-O_O$ second neighbors).

The coordination number (N), Debye–Waller factor (σ^2), distance (R) and energy shift (E_0), together with the number of independent variables for every fit (V) and their agreement factor ($\Delta\chi^2$), are shown. The best fits are shown with an asterisk.

Natural schwertmannite.

Model	Neighbor	Path	N (atoms)	σ^2 (Å^{-2})	R (Å)	ΔE_0 (eV)	V	$\Delta\chi^2$
1	One shell	$S-O_T$	3.800 (fixed)	0.0004 ± 0.0001	1.483 ± 0.003	14.033 ± 0.967	8	26.8
2	Shell 1	$S-O_T$	3.800 (fixed)	0.0003 ± 0.0003	1.489 ± 0.003	11.968 ± 0.684	6	21.4
	Shell 2	$S-Fe$	0.150 (fixed)	0.0026 ± 0.0036	3.208 ± 0.392	11.968 ± 0.684		
3*	Shell 1	$S-O_T$	3.756 ± 0.026	0.0002 ± 0.0003	1.479 ± 0.002	13.800 ± 0.847	4	11.5
	Shell 2	$S-O_O$	3.114 ± 0.054	0.0080 ± 0.0057	2.415 ± 0.027	13.800 ± 0.847		
	Shell 3	$S-Fe_T$	2.232 ± 0.105	0.0149 ± 0.0037	2.865 ± 0.042	13.800 ± 0.847		

Synthetic schwertmannite.

Model	Neighbor		N (atoms)	σ^2 (Å^{-2})	R (Å)	ΔE_0 (eV)	V	$\Delta\chi^2$
1	One shell	$S-O_T$	3.840 (fixed)	0.0001 ± 0.0001	1.486 ± 0.002	15.333 ± 2.260	8	35.0
2	Shell 1	$S-O_T$	3.840 (fixed)	0.0001 ± 0.0001	1.486 ± 0.002	14.223 ± 1.052	6	27.7
	Shell 2	$S-Fe$	1.160 (fixed)	0.0001 ± 0.0001	2.789 ± 0.036	14.223 ± 1.052		
3*	Shell 1	$S-O_T$	3.880 ± 0.025	0.0001 ± 0.0002	1.487 ± 0.004	15.649 ± 1.962	6	20.8
	Shell 2	$S-O_O$	1.012 ± 0.146	0.0050 ± 0.0069	2.441 ± 0.056	15.649 ± 1.962		
	Shell 3	$S-Fe$	1.702 ± 0.068	0.0093 ± 0.0029	2.851 ± 0.027	15.649 ± 1.962		

Table 2
Agreement parameter R_w of the Rietveld refinements of the studied samples with and without the presence of goethite.

	SynHT	Syn	Nat-Air	Nat-Freeze
R_w with goethite (%)	4.6	5.3	4.7	5.3
R_w without goethite (%)	9.1	5.8	4.8	5.4

Table 3
Amounts of goethite and schwertmannite found by Rietveld refinements for the studied samples in the fits considering the presence of goethite.

	SynHT	Syn	Nat-Air	Nat-Freeze
Goethite ($w/w\%$)	26	14	13	13
Schwertmannite ($w/w\%$)	74	86	87	87

for this could be the lack of the multiple scattering path $S-O-O$ within the SO_4 tetrahedron in the fits. However, while the inclusion of an inner-sphere monodentate model improved the R factor of all the fits, F-test statistical data analyses showed that this hypothesis yielded a confidence level higher than 90% only for synthetic schwertmannite (see Table S1). This result implies that, although XANES indicates that IS sulfate is present in schwertmannite, the presence of a second shell in the EXAFS data is not statistically significant.

4.2. Rietveld analysis

Experimental and fitted diffraction patterns are reported in Fig. 3, as well as the relative contributions of each phase

(schwertmannite and goethite), and values of the refined parameters are shown in Tables 2–4. It can be noted that a peak emerges at 3° 2θ ($Q = 1.5$ Å^{-1}), whose intensity varies from pattern to pattern of the four different samples. This peak is completely recognizable in the pattern of the sample SynHT, while it appears as a small shoulder in the patterns of the samples Syn and Nat-Air. The pattern of Nat-Freeze apparently does not show any contribution. This peak is not related to the cell proposed for schwertmannite, and it corresponds to the 101 reflection of goethite. Two different types of refinements were thus conducted, with and without goethite. Values of the agreement parameter R_w (%) for each of the different Rietveld refinement fits are given in Table 2. The addition of goethite yields a better result in all of the studied cases. This is clear for the SynHT sample, for which the goethite concentration is the highest (results of the quantitative phase analysis by Rietveld refinement are given in Table 3). Regarding the sample SynHT, the presence of goethite not only is required in order to reproduce the peak at $2\theta = 3°$ but also results in the improvement of the intensity of the peaks at 5° and, though to a lesser extent, the reflections at 3.75 and 6.25°. As previously stated, the peak at 3° appears less intense in the remaining patterns. In the samples Syn and Nat-Air this peak can be distinguished as a shoulder of the peak at $2\theta = 2.5°$, while in the sample Nat-Freeze it is not distinguishable at all. This behavior is in agreement with the values found for the concentration of goethite (Table 3), which progressively decreases from the sample SynHT to the sample Nat-Freeze. Although not distinctly observable in the pattern of the sample Nat-Freeze, the presence of goethite ensures the perfect reproduction of the peak shape. The domain size does not significantly change during the refinement process. Taking into account the error that can be produced by considering surface effects and disorder, all the values, around ~40 Å, can be considered to be in accordance with the literature (French *et al.*, 2012).

With respect to the cell parameters, comparable results are found for the schwertmannite unit cell, which do not considerably change from the starting values.

Refinement of the sulfate occupancy did not result in any improvement of results. The sulfate inner/outer ratio has implications for the ratio of the intensity of the peaks at $2\theta = 2.5°$ and $2\theta = 3.75°$. The intensity of these peaks was well reproduced before considering the sulfate occupancy as a refinable parameter. The starting inner/outer ratio $\simeq 1$ yielded a good fit and it did not vary during the refinement procedure.

As a further test on the effect of the IS/OS ratio, a sensitivity analysis was conducted, imposing on the schwertmannite
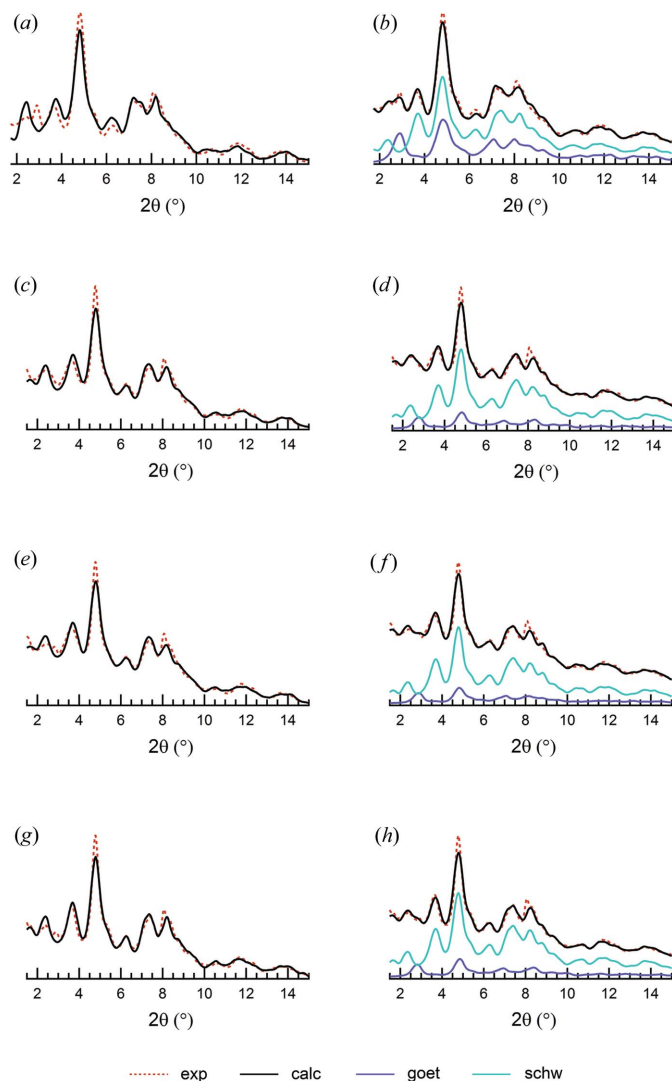
Figure 3
Rietveld refinement results for (a) sample SynHT with goethite, (b) sample SynHT without goethite, (c) sample Syn with goethite, (d) sample Syn without goethite, (e) sample Nat-Air with goethite, (f) sample Nat-Air without goethite, (g) sample Nat-Freeze with goethite and (h) sample Nat-Freeze without goethite.
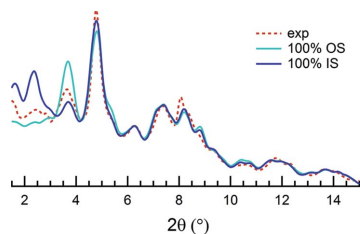

Figure 4
Sensitivity analysis on the IS/OS ratio. The intensities of the reflections at $2\theta = 2.5$ and $3.8°$ are sensitive to the IS/OS ratio. The experimental pattern (sample Nat-Air) has intensity values between the values of the calculated diffraction patterns for 100% IS sulfate and 100% OS sulfate.

Table 4
Parameters found by Rietveld refinements for the studied samples in the fits considering the presence of goethite.

Parameter	SynHT	Syn	Nat-Air	Nat-Freeze	Starting
Particle size goethite (Å)	59	40	40	40	40
Particle size schwertmannite (Å)	44	48	40	40	40
Cell goethite					
a (Å)	10.00	9.67	9.59	9.60	9.91
b (Å)	3.02	3.08	3.11	3.13	3.01
c (Å)	4.61	4.46	4.43	4.43	4.58
Cell schwertmannite					
a (Å)	10.49	10.53	10.56	10.66	10.59
b (Å)	6.02	6.06	6.08	6.09	6.06
c (Å)	10.30	10.49	10.42	10.43	10.51
α (°)	92	91	90	90	90
β (°)	85	86	86	87	87
γ (°)	89	89	90	90	90
Sulfate occupancy					
Inner sphere	2.3	2.3	2	2.4	2
Outer sphere	1.7	1.7	2	1.6	2

cell the presence of 100% IS or the presence of 100% OS. As shown in Fig. 4, the intensity of the peaks at $2\theta = 2.5°$ and $2\theta = 3.8°$, which are sensitive to the IS/OS ratio, falls between the intensities of the two calculated patterns.

Differences between calculated and experimental patterns remain after the refinement procedure. They concern the peaks at $2\theta = 5°$ in all of the studied patterns, whose intensity is not well reproduced especially for the samples Syn, Nat-Air and Nat-Freeze, and the peak at $2\theta = 8°$, whose shape is not well reproduced.

4.3. RMC/DSE analysis

RMC/DSE analysis was conducted in order to obtain a three-dimensional finite size particle representative of the structure of schwertmannite and to fine-tune the short-range order of these nanoparticles, so the previously mentioned differences are accounted for. Reciprocal- and real-space data from samples SynHT and Nat-Freeze – the two samples showing more and less goethite content, respectively – were used in order to perform a quantitative analysis. For each sample two refinements were conducted: in the first refinement only a 30 Å spherical particle built from the modified Bigham cell was considered; in the second also a 30 Å spherical particle of goethite was refined. In the latter case, the amount of goethite content was evaluated before RMC analysis by applying linear combination analyses to $S(Q)$. The resulting calculated $S(Q)$ is then a weighted sum of the $S(Q)$s calculated from goethite and schwertmannite particles, which are both shown in Fig. 5 together with the experimental $S(Q)$ of the SynHT sample. The PDF is obtained by applying the FT up to the value of $Q_{max} = 25$ Å^{-1} for the sample SynHT and $Q_{max} = 18$ Å^{-1} for the sample Nat-Freeze.

The results from XAS, Rietveld refinement and the sensitivity analysis shown in Fig. 4 converge towards an IS/OS ratio
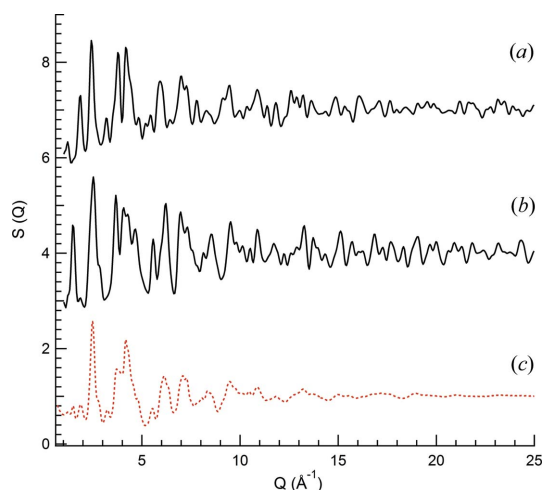
Figure 5
$S(Q)$s calculated for (a) the Bigham model particle (30 Å diameter) (black) and (b) the goethite model particle (black) compared with (c) the experimental $S(Q)$ of the sample SynHT of schwertmannite (red dotted).
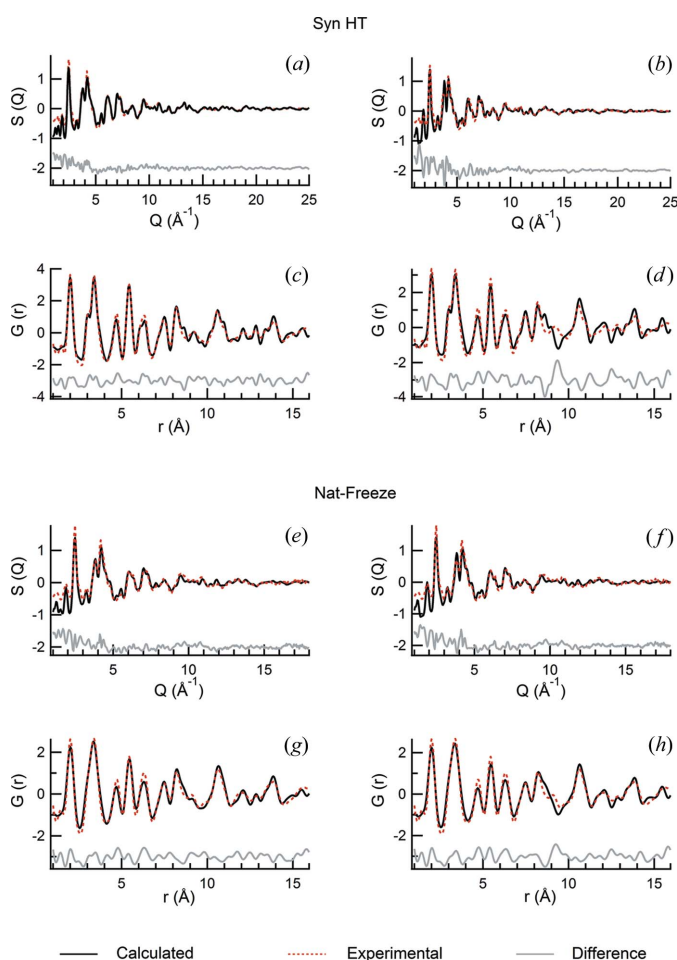

Figure 6
RMC fits for samples (a)–(d) SynHT (top) and (e)–(h) Nat-Freeze (bottom): $S(q)$ fits performed considering the presence of goethite (a), (e) and using calculated diffraction data only from the Bigham particle model (b), (f); PDF fits performed considering the presence of goethite (c), (g) and using calculated diffraction data only from the Bigham particle model (d), (h).

close to 1. Consequently, this value was not refined during the RMC/DSE analysis. In Fig. 6 the result of the RMC/DSE fits for the SynHT and Nat-Freeze samples in the presence and absence of goethite are shown. The amount of goethite found by linear fitting is in agreement with the results obtained by Rietveld refinement, with 30% of goethite estimated for the SynHT sample data and 18% of goethite estimated for the Nat-Freeze sample data.

The profile of the $S(Q)$s and the PDFs is adequately reproduced but, as in the case of the Rietveld analysis, the presence of goethite ensures better agreement with the experimental data, both for the SynHT sample and for the Nat-Freeze sample.

Looking at the $S(Q)$s the presence of goethite guarantees a better agreement in the Q range from 1 to 2 Å^{-1} and for the peak at $Q = 3.5$ Å^{-1}, whose intensity is sensitive to the presence of goethite.

It is interesting to highlight the results of the PDF fits, which are complementary to the results obtained in the reciprocal space with the $S(Q)$s refined with RMC/DSE and with the diffraction patterns refined with Rietveld analysis. The main differences between the refinements conducted in the absence and presence of goethite concern the range $r = 8$–10 Å, with the goethite allowing a better agreement between the experimental and the calculated data. The study of this region of the PDF looks like an alternative tool to the identification of the peak at $Q = 1.5$ A^{-1} in the diffraction pattern in order to estimate the presence, and conceivably the amount, of goethite. For a deeper understanding of the influence of goethite, the partial contributions of goethite and of the structure made up of the Bigham cell to the PDF are shown in Fig. 7.

The physical consistency of the models obtained by RMC/DSE analysis is ensured by the constraints imposed on the minimum distances between pairs of atoms. A histogram of the first distances between the atoms in the schwertmannite and goethite particles is shown in Fig. 8, while the three-
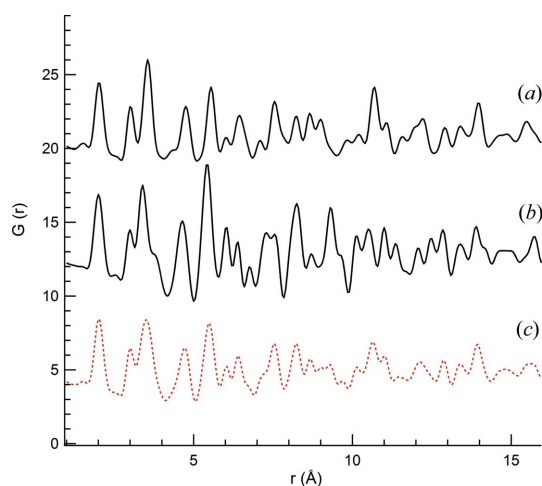

Figure 7
PDFs calculated for (a) the Bigham model particle (30 Å diameter) (black) and (b) the goethite model particle (black) compared with (c) the experimental PDF of the sample SynHT of schwertmannite (red dotted).
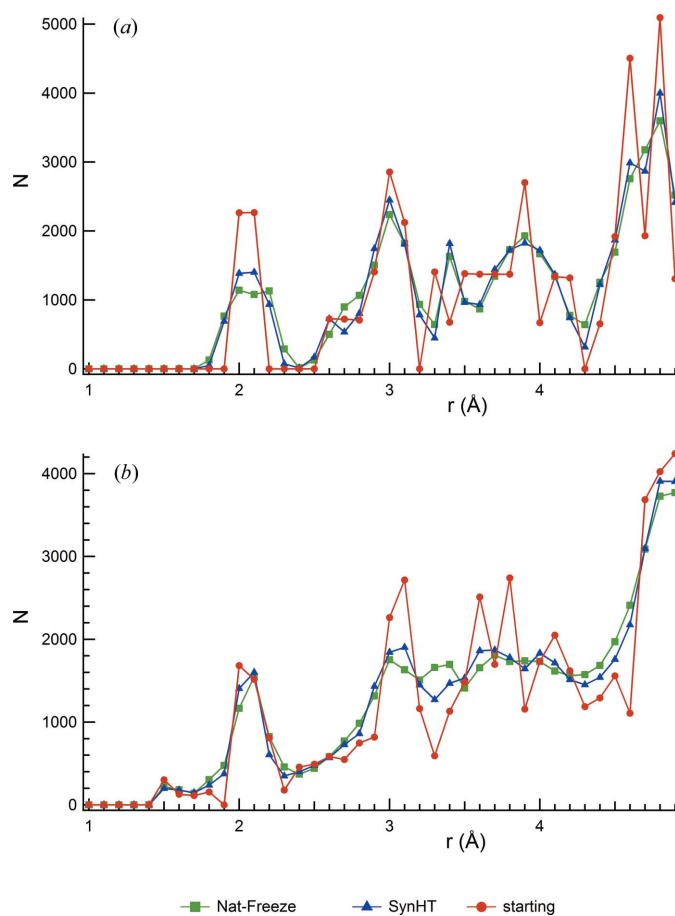
Figure 8
Histogram of distances corresponding to the closest pairs of atoms in (b) the Bigham model particle and (a) the goethite model particle. Distances of the two models before RMC analysis starts (red, circles), distances obtained refining the SynHT sample (blue, triangles) and distances obtained refining the Nat-Freeze sample (green, squares) are reported.
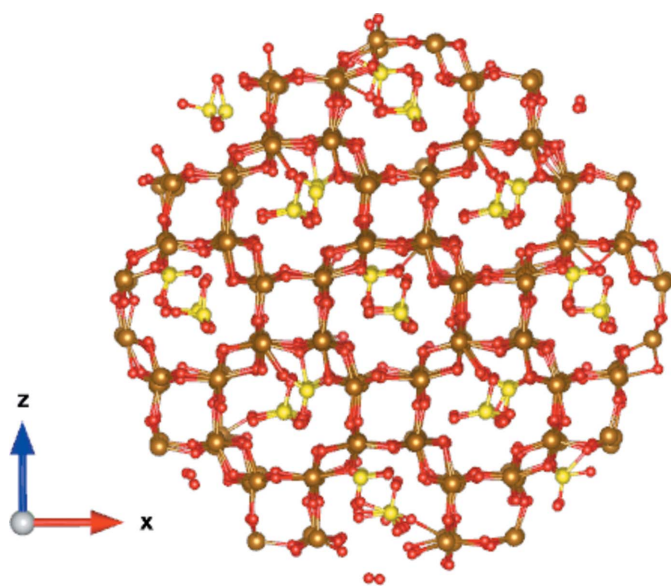

Figure 9
Three-dimensional particle model for schwertmannite obtained after the RMC refinement of the Bigham model. Red spheres are O atoms, brown spheres are Fe atoms and yellow spheres are S atoms.

dimensional structure of the particle of schwertmannite obtained by refining the SynHT sample data is shown in Fig. 9.

5. Conclusions

The case of schwertmannite is probably one of the most paradigmatic examples of (i) the limitation of traditional 'Bragg scattering' techniques to elucidate the nanostructure of mineral nanoparticles; (ii) the advantages of total scattering techniques to obtain information from the diffuse scattering; but, most importantly (iii) the need of a combined analysis of diffuse and Bragg components, using highly constrained modeling approaches such as the one shown here. Our results show unequivocally that the presence of goethite in schwertmannite samples can be hidden in the diffuse scattering of the diffraction pattern and can be difficult to detect with conventional techniques. This result highlights the need for total scattering characterization techniques that also integrate the diffuse scattering component of the patterns. Moreover, the combined RMC/DSE models developed here have allowed refinement of the structure of schwertmannite using a whole nanoparticle model. This approach allows the 'creation' of different types of disorder in a statistical way such that the configurational space is explored more efficiently. Also, the occupation of the sulfate positions and their refinement during RMC/DSE cycles, combined with the S K-edge XANES information provided, confirm that sulfate is present in at least two different configurations, with both outer-sphere and inner-sphere ligands.

The fact that a fraction of goethite is present even in schwertmannite samples that show only the characteristic schwertmannite diffraction peaks in their powder diffraction pattern has potentially important implications. A recent study by Caraballo *et al.* (2013) showed that schwertmannite has a wide range of solubility products (log K_{sp}), ranging from 5.8 to 39.5. Could at least part of this difference be explained by the presence of goethite domains within the schwertmannite samples under study, not detected by conventional XRD? Indeed, a visual inspection of Fig. 1 of Caraballo *et al.* (2013) allows a small goethite peak to be identified in one of the patterns (second from the top, at around $2\theta \simeq 22°$).

Here, the presence of goethite has been accounted for in the model by adding a goethite nanoparticle contribution to the scattering data. Although this approach gives a good result, more elaborate models could be envisaged in which the goethite contribution is 'embedded' in the structural network of a schwertmannite nanoparticle. Such a molecular model would need to include a lattice with some orders of freedom and refinable parameters such as site occupations. The non-stoichiometric topotactic transformation from schwertmannite to goethite provides a good basis for the construction of such a model, although this is out of the scope of the present work. The schwertmannite model presented here is so far, to the authors' knowledge, the most complete model reported, using various sources of data. This model is expected to be useful for molecular geochemistry studies addressing the study

of the interactions of anionic pollutants with this enigmatic mineral.

References

Antonov, L. D., Andreetta, C. & Hamelryck, T. (2012). *Proceedings of the International Conference on Bioinformatics Models, Methods and Algorithms*, pp. 102–108. Vilamoura: SciTePress – Science and Technology Publications.

Barla, A., Nicolás, J., Cocco, D., Valvidares, S. M., Herrero-Martín, J., Gargiani, P., Moldes, J., Ruget, C., Pellegrin, E. & Ferrer, S. (2016). *J. Synchrotron Rad.* **23**, 1507–1517.

Bigham, J. M., Carlson, L. & Murad, E. (1994). *Mineral. Mag.* **58**, 641–648.

Bigham, J. M., Schwertmann, U., Carlson, L. & Murad, E. (1990). *Geochim. Cosmochim. Acta*, **54**, 2743–2758.

Bigham, J. M., Schwertmann, U., Traina, S. J., Winland, R. L. & Wolf, M. (1996). *Geochim. Cosmochim. Acta*, **60**, 2111–2121.

Billinge, S. J. L. & Kanatzidis, M. G. (2004). *Chem. Commun.* **2004**, 749–760.

Burton, E. D., Bush, R. T., Sullivan, L. A. & Mitchell, D. R. G. (2008). *Geochim. Cosmochim. Acta*, **72**, 4551–4564.

Caraballo, M. A., Michel, F. M. & Hochella, M. F. (2015). *Am. Mineral.* **100**, 14–25.

Caraballo, M. A., Rimstidt, J. D., Macías, F., Nieto, J. M. & Hochella, M. F. (2013). *Chem. Geol.* **360–361**, 22–31.

Cervellino, A., Giannini, C. & Guagliardi, A. (2003). *J. Appl. Cryst.* **36**, 1148–1158.

Cervellino, A., Giannini, C. & Guagliardi, A. (2006). *J. Comput. Chem.* **27**, 995–1008.

Cicco, A., Aquilanti, G., Minicucci, M., Principi, E., Novello, N., Cognigni, A. & Olivi, L. (2009). *J. Phys. Conf. Ser.* **190**, 012043.

Debye, P. (1915). *Ann. Phys.* **351**, 809–823.

Deore, S. W., Mazeina, L., Navrotsky, A., Tamura, N. & Fakra, S. (2005). *Geochim. Cosmochim. Acta*, **69**, A806.

Egami, T. & Billinge, S. J. L. (2003). *Underneath the Bragg Peaks: Structural Analysis of Complex Materials*. Oxford: Pergamon, Elsevier.

Fernandez-Martinez, A., Timon, V., Román-Ross, G., Cuello, G. J., Daniels, J. E. & Ayora, C. (2010). *Am. Mineral.* **95**, 1312–1322.

Ferrari, M. & Lutterotti, L. (1994). *J. Appl. Phys.* **76**, 7246–7255.

French, R. A., Caraballo, M. A., Kim, B., Rimstidt, J. D., Murayama, M. & Hochella, M. F. (2012). *Am. Mineral.* **97**, 1469–1482.

French, R. A., Monsegue, N., Murayama, M. & Hochella, M. F. (2014). *Phys. Chem. Miner.* **41**, 237–246.

Galassi, M., Davies, J., Theiler, J., Gough, B., Jungman, G., Alken, P., Booth, M. & Rossi, F. (2009). GNU Scientific Library Reference Manual. Network Theory Ltd.

Gelisio, L., Azanza Ricardo, C. L., Leoni, M. & Scardi, P. (2010). *J. Appl. Cryst.* **43**, 647–653.

Gilbert, B., Erbs, J. J., Penn, R. L., Petkov, V., Spagnoli, D. & Waychunas, G. A. (2013). *Am. Mineral.* **98**, 1465–1476.

Gualtieri, A. & Venturelli, P. (1999). *Am. Mineral.* **84**, 895–904.

Hall, B. D. (2000). *J. Appl. Phys.* **87**, 1666–1675.

Hammersley, A. P. (2016). *J. Appl. Cryst.* **49**, 646–652.

Hammersley, A. P., Svensson, S. O., Hanfland, M., Fitch, A. N. & Häusermann, D. (1996). *High Pressure Res.* **14**, 235–248.

Hockridge, J. G., Jones, F., Loan, M. & Richmond, W. R. (2009). *J. Cryst. Growth*, **311**, 3876–3882.

Joyner, R. W., Martin, K. J. & Meehan, P. (1987). *J. Phys. C Solid State Phys.* **20**, 4005–4012.

Kawano, M. & Tomita, K. (2001). *Am. Mineral.* **86**, 1156–1165.

Loan, M., Cowley, J. M., Hart, R. & Parkinson, G. M. (2004). *Am. Mineral.* **89**, 1735–1742.

McGreevy, R. L. & Pusztai, L. (1988). *Mol. Simul.* **1**, 359–367.

Michalowicz, A., Provost, K., Laruelle, S., Mimouni, A. & Vlaic, G. (1999). *J. Synchrotron Rad.* **6**, 233–235.

Myneni, S. C. B. (2000). *Rev. Mineral. Geochem.* **40**, 113–172.

Newville, M. (2001). *J. Synchrotron Rad.* **8**, 322–324.

Qiu, X., Thompson, J. W. & Billinge, S. J. L. (2004). *J. Appl. Cryst.* **37**, 678.

Ravel, B. & Newville, M. (2005). *J. Synchrotron Rad.* **12**, 537–541.

Regenspurg, S., Brand, A. & Peiffer, S. (2004). *Geochim. Cosmochim. Acta*, **68**, 1185–1197.

Rietveld, H. M. (1969). *J. Appl. Cryst.* **2**, 65–71.

Sánchez-España, J., Yusta, I. & Diez-Ercilla, M. (2011). *Appl. Geochem.* **26**, 1752–1774.

Schwertmann, U. & Cornell, R. M. (1991). *Iron Oxides in the Laboratory: Preparation and Characterization*. Weinheim: Wiley-VCH.

Wang, H., Bigham, J. M. & Tuovinen, O. H. (2006). *Mater. Sci. Eng. C*, **26**, 588–592.

Wang, X., Gu, C., Feng, X. & Zhu, M. (2015). *Environ. Sci. Technol.* **49**, 10440–10448.

Yu, J. Y., Heo, B., Choi, I. K., Cho, J. P. & Chang, H. W. (1999). *Geochim. Cosmochim. Acta*, **63**, 3407–3416.